DOI: 10.15480/882.9429

Eighth International Symposium on Marine Propulsors
smp'24, Berlin, Germany, March 2024

Approaches for Performance Prediction of Marine Propellers under Open Water Test Conditions using the Boundary Element Method *

Robert Beckmann[1], Raphael Bévand[1], Nino Grosjean[2], Ulf Göttsche[1], Moustafa Abdel-Maksoud[1]

[1]Institute for Fluid Dynamics and Ship Theory, Hamburg University of Technology (TUHH), Germany
[2]INP ENSEEIHT, Toulouse, France

ABSTRACT

Open water test predictions with boundary element methods suffer from the fact, that the predicted thrust and torque coefficient at low advance ratios are often not well predicted. This is mainly explained by the missing viscous influence in potential flow theory. Additionally, the accurate computation of surface gradients needed for the pressure distribution is challenging for highly skewed panels. Therefore, in this paper, different approaches are investigated for two representative propellers openly available in the research community; the INSEAN E779A propeller and the Potsdam Propeller Test Case (PPTC). The focus lies in the study, how an unstructured grid with optional consideration of the propeller hub geometry can improve the open water characteristics. First, the chosen mesh topology is described, followed by an assessment of different surface gradient reconstruction approaches for the structured and unstructured grid. Then, open water simulations for different structured and unstructured grids are carried out and the influence of the linear and the nonlinear Kutta condition is discussed on the overall open water characteristics as well as on the pressure distribution in detail. A summary and an outlook is given regarding the capabilities and limitations of unstructured grids and suggestions for further improvements.

Keywords

boundary element method, marine propeller, mesh topology, surface gradient, nonlinear Kutta condition

1 INTRODUCTION

To assess the performance of a propeller, open water tests are carried out in uniform inflow condition at experimental facilities. During the design stage, preliminary propeller geometries are investigated for their optimal shape. During this stage, numerical procedures are an attractive alternative with respect to time consuming and costly experiments.

Established numerical methods for this purpose are viscous *Reynolds-Averaged Navier-Stokes* (RANS) methods and boundary element methods (BEM). The latter are numerically more efficient because they do not resolve the entire fluid volume but only the boundary surface of the propeller geometry. However, due to simplifications made by these methods with respect to the governing equations of fluid dynamics, viscous effects can not be captured and numerical stability challenges may arise related to the employed singularity distributions and the flow at the blade's trailing edge. The latter can be iteratively corrected with a nonlinear Kutta condition (Wang & Abdel-Maksoud et al. 2017a) to achieve a zero pressure difference at the trailing edge. For highly loaded blades at the tip this can lead to stability issues and often a large portion of the blade tip is trimmed to maintain the stability of the solution.

This paper aims to explore how numerical open water predictions can be improved with a boundary element method. The focus lies on the use of alternative unstructured grid topologies, since as of the knowledge of the authors, structured grids are often applied. Therefore, the following topics are discussed: the prediction accuracy of the surface gradients involved in the pressure prediction, the influence of the hub geometry on the pressure distribution in connection with the linear and nonlinear Kutta conditions.

2 THEORY

In this section, an overview of the theory applied with references to literature is given.

2.1 Boundary Element Method

In this study, the boundary element method *pan*MARE is applied, which is developed at the Institute for Fluid Dynamics and Ship Theory, Hamburg University of Technology (Hundemer 2013). The fluid flow is assumed to be inviscid and irrotational. With these assumptions a scalar velocity potential $\Phi(\boldsymbol{x}) = \Phi(x, y, z)$ can be derived, for which the velocity field results from its gradient. The governing equations of mass conservation and momentum conservation become the Laplace equation and the Bernoulli equation, respectively:

$$\Delta\Phi = \nabla \cdot \nabla\Phi = 0 \,, \tag{1a}$$

$$\frac{p}{\rho} + \boldsymbol{g} \cdot \boldsymbol{x} + \frac{1}{2}|\boldsymbol{v}|^2 + \frac{\partial\Phi}{\partial t} = \text{const} \,. \tag{1b}$$

Due to the linearity of the potential, it is expressed as the sum of elementary solutions. In *pan*MARE, a panelwise

constant source strength distribution σ and a constant doublet strength distribution μ is employed. Further details of the underlying theory are given by Joseph Katz (2010) with respect to e.g. the evaluation of induced velocities by each panel. To avoid singularity evaluations close to each panel edge, a desingularization radius r_δ for the doublet strength is used. Given the direction vectors of the edge $\boldsymbol{r}_E$ and between the edge corners and the evaluation point $\boldsymbol{r}_A$, $\boldsymbol{r}_B$ as well as the circulation Γ (doublet strength difference between adjacent panels), the induced (desingularized) velocity can be computed as:

$$\boldsymbol{v} = \frac{\Gamma}{4\pi}\,\boldsymbol{r}_E \cdot \left(\frac{\boldsymbol{r}_A}{|\boldsymbol{r}_A|} - \frac{\boldsymbol{r}_B}{|\boldsymbol{r}_B|}\right) \frac{\boldsymbol{r}_A \times \boldsymbol{r}_B}{|\boldsymbol{r}_A \times \boldsymbol{r}_B|^2}\,, \tag{2a}$$

$$\boldsymbol{v}_{\mathrm{des}} = \left[1 - \exp\left(\frac{r^2}{r_\delta^2}\right)\right] \boldsymbol{v}\,. \tag{2b}$$

The desingularization radius is kept constant for the entire wake. An alternative approach, which exhibits a better roll-up behavior of the free shear sheet further downstream and where r_δ varies with the vortex age, is described by Wang et al. (2016).

To predict viscous forces on the blade the method developed by Schlichting (1979) is applied. The local Reynolds number Re is evaluated by calculating streamlines upstream to the pressure stagnation point.

2.2 Open Water Characteristics

The open water characteristics provide useful insights of the propeller performance in uniform inflow condition as a function of the advance ratio $J = \frac{V_A}{nD}$, expressed by the thrust coefficient k_T, the torque coefficient k_Q, and the open water efficiency η_O:

$$k_T = \frac{T}{\rho n^2 D^4}\,,\; k_Q = \frac{Q}{\rho n^2 D^5}\,,\; \eta_O = \frac{J}{2\pi}\frac{k_T}{k_Q}\,. \tag{3}$$

For comparison between experimental and numerical results, the relative error $\varepsilon_{\mathrm{rel}}(k_T)$ and $\varepsilon_{\mathrm{rel}}(k_Q)$ is expressed with respect to the design point thrust and torque coefficient for each propeller, i.e.:

$$\varepsilon_{\mathrm{rel}}(k_T) = \frac{k_T(J) - k_{T,\mathrm{exp}}(J)}{k_{T,\mathrm{exp}}(J_{\mathrm{Design}})}\,, \tag{4a}$$

$$\varepsilon_{\mathrm{rel}}(k_Q) = \frac{k_Q(J) - k_{Q,\mathrm{exp}}(J)}{k_{Q,\mathrm{exp}}(J_{\mathrm{Design}})}\,. \tag{4b}$$

The pressure distribution on the profiles is expressed as the pressure coefficient c_p, normalized by the free stream velocity and the blade tip rotatory velocity:

$$c_p = \frac{2(p - p_{\mathrm{ref}})}{\rho\,(V_A^2 + (\pi n D)^2)}\,. \tag{5}$$

2.3 Grid Generation

This section provides an overview of the meshing techniques employed. A comparison between structured and unstructured grids approach is given.

Two algorithms for generating unstructured grids, namely the hyperbolic extrusion and the advancing front method, are applied. Both rely on projection procedures, which determine the nearest grid point on the boundary surface. For certain propeller geometries or in regions of extremely high curvature, the projection can be challenging to converge.

2.3.1 Hyperbolic Extrapolation

This algorithm extrapolates a marching front based on an initial boundary curve in locally orthogonal direction in-plane to the surface based on the description of Chan & Buning (1994). The governing grid generation equation system is derived using local boundary curve tangent vectors $\boldsymbol{r}_\xi$, $\boldsymbol{r}_\eta$ and the normal surface vector $\hat{\boldsymbol{n}}$:

$$\boldsymbol{r}_\xi \cdot \boldsymbol{r}_\eta = 0\,, \tag{6a}$$

$$\hat{\boldsymbol{n}} \cdot (\boldsymbol{r}_\xi \times \boldsymbol{r}_\eta) = \Delta S\,, \tag{6b}$$

$$\hat{\boldsymbol{n}} \cdot \boldsymbol{r}_\eta = 0\,. \tag{6c}$$

The subscripts ξ and η denote the directions tangential and normal to the marching front, respectively. The mesh cell size ΔS is a function of the marching step. In this study, it is chosen to vary exponentially for each marching layer. The local tangent vectors are expressed as central finite differences while the surface normal is evaluated analytically.

2.3.2 Advancing Front Method

This algorithm is used to fill the remaining surface area with panels based on the methodology described by Rypl & Bittnar (1996). Similar to the hyperbolic algorithm, an initial boundary is required. Based on the initial front, new point candidates are inserted with respect to the center of each boundary edge with an offset normal to the boundary. New triangular panel corners are selected based on geometric constraints. Either by selecting new points which yield an optimal triangle shape, or by snapping to existing points using spherical or ellipsoid catch radii.

2.4 Surface Gradient

After solving the Dirichlet boundary condition, the discrete source strengths σ and doublet strengths μ are known for each panel. Subsequently, the induced velocity components are computed to obtain the pressure distribution on the body surface. The normal component is already given by the source strength, while the tangential components have to be reconstructed from the surface gradient of the doublet strength. For each panel, a polynomial ansatz function is formulated in its local frame of reference (ξ, η). Considering n neighbour panels, a linear equation system is solved to obtain the vector $\boldsymbol{\delta}$ with m polynomial coefficients:

$$\boldsymbol{A}\boldsymbol{\delta} = \boldsymbol{y}, \quad \text{with} \quad \boldsymbol{A} \in \mathbb{R}^{n\times m}\,, \boldsymbol{\delta} \in \mathbb{R}^m\,, \boldsymbol{y} \in \mathbb{R}^n\,. \tag{7}$$

The coefficient matrix $\boldsymbol{A}$ is given by the product of a diagonal weight matrix $\boldsymbol{W}$ with a distance matrix $\boldsymbol{D}$, and the right hand side elements y_i represent the weighted difference between the known doublet strengths $\mu_i = \mu(\xi_i, \eta_i)$ and μ_0 of the i-th neighbour panel and the panel of interest, respectively:

$$\boldsymbol{A} = \boldsymbol{W}\boldsymbol{D}, \quad \text{with} \quad \boldsymbol{W} \in \mathbb{R}^{n\times n}\,, \boldsymbol{D} \in \mathbb{R}^{n\times m}\,, \tag{8}$$

$$y_i = W_{ii}\,(\mu_i - \mu_0)\,, \quad i = 1, \ldots, n\,. \tag{9}$$

The diagonal elements of the weight matrix are either $W_{ii} = 1$ or equal to an arbitrary power p of the distance r_i^p between each panel pair. The rows in the distance matrix follow from the chosen polynomial function. In *pan*MARE, linear, bilinear, quadratic, and biquadratic polynomials are implemented. Their distance matrix row vectors are, respectively:

$$D_i = [\xi_i,\ \eta_i,] \ , \tag{10a}$$
$$D_i = [\xi_i,\ \eta_i,\ \xi_i\eta_i,] \ , \tag{10b}$$
$$D_i = \left[\xi_i,\ \eta_i,\ \xi_i^2,\ \eta_i^2\right] \ , \tag{10c}$$
$$D_i = \left[\xi_i,\ \eta_i,\ \xi_i^2,\ \eta_i^2,\ \xi_i\eta_i,\ \xi_i^2\eta_i,\ \xi_i\eta_i^2,\ \xi_i^2\eta_i^2\right] \ . \tag{10d}$$

If the number of neighbours n is greater than the number of equations m, a least square minimization problem is solved in form of the *normal equation*:

$$\boldsymbol{A}^T\boldsymbol{A}\,\boldsymbol{x} = \boldsymbol{A}^T\boldsymbol{y} \ . \tag{11}$$

Otherwise, if the number of neighbours for a given polynomial is too small in absolute terms or along a direction (ξ or η), then the incalculable terms are removed.

For triangular or quadrilateral panels, three or four direct panel neighbours can be found along the panel edges. By default, *pan*MARE employs a quadratic polynomial. Optionally, also the adjacent panels sharing a panel corner may be included as neighbours.

3 TEST CASES

The investigations conducted are based on two test cases: the *Potsdam Propeller Test Case* (PPTC) (Potsdam 2011) and the *INSEAN Propeller E779A* (Salvatore et al. 2006).

The E779A propeller has a diameter of $D = 0.227\,27\,\mathrm{m}$ and a relative hub diameter of $d_h/D = 0.2003$. The propeller operates in the open water test with a rotation rate of $n = 11.7881\ 1/\mathrm{s}$. The design advance ratio is $J_{\mathrm{Design}} = 0.88$ resulting in reference values of $k_{T,\mathrm{exp}} = 0.157$ and $k_{Q,\mathrm{exp}} = 0.031$.

The PPTC propeller has a diameter of $D = 0.25\,\mathrm{m}$ and a relative hub diameter of $d_h/D = 0.3$. The propeller operates with a rotation rate of $n = 15\ 1/\mathrm{s}$. The design advance ratio is $J_{\mathrm{Design}} = 1.019$ resulting in experimental reference values of $k_{T,\mathrm{exp}} = 0.389$ and $k_{Q,\mathrm{exp}} = 0.096$.

The propeller flow simulations are made for a set of structured grids with increasing chord-wise (NC) and span-wise (NS) resolution. These are given by 24×16, 32×24, 40×28 and 48×28. One unstructured grid is tested.

3.1 Grid

On the propeller blade, the initial boundary curve for the meshing process of the unstructured grid, as introduced in Section 3, is defined by the geometric leading edge, blade tip, and trailing edge. A separate number of grid points is distributed on these boundary curves. The profile curvature is well resolved with homogeneous aspect ratio, avoiding highly skewed panels. Theoretically, this topology is applicable for a wide range of propeller geometries, especially for highly skewed blades.

For the hub surface, the intersection curve between blade and hub surface is chosen as initial boundary curve. This results in structured quadrilateral orthogonal panels, which are favorable for gradient computations. This grid is well adapted to the shape of the intersection curve. The extrapolation distance is chosen such that enough space is kept between the periodic boundary and the final marching front.

The geometry of the E779A propeller is depicted in Figure 1 for a structured and an unstructured topology. The red line at the relative radius $r/R = 0.264$ indicates the smallest radius given in Salvatore et al. (2006). The missing radial cut is extrapolated towards the hub surface. The blade tip is trimmed at an relative radius of $r/R = 0.9975$ for the structured grid and at a relative radius of $r/R = 0.9950$ for the unstructured grid.

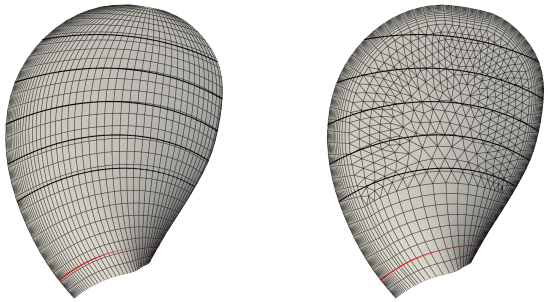

(a) Structured grid **(b) Unstructured grid**

Figure 1: E779A Topologies

While the hyperbolic method is relatively insensitive regarding the mesh size along the front, the advancing front method allows only moderate changes in mesh size to achieve well shaped triangles and to capture the surface curvature with satisfying accuracy. Keeping these aspects in mind, the blade surface is meshed by multiple grid blocks. At the hub region, the blade is meshed by a H-grid.

For comparison of the results with and without hub, the blade is cut for both cases at the given hub diameter. Cylindrical sections at the non-dimensional radii $[0.5, 0.6, 0.7, 0.8, 0.9]$ are shown as reference curves in black color. Additionally, Figure 2 depicts an optional panel coarsening at the trailing edge. Coarsening is applied because the fine resolution in chord direction introduces conditioning issues in the equation system with respect to the nonlinear Kutta condition as discussed in Section 4.

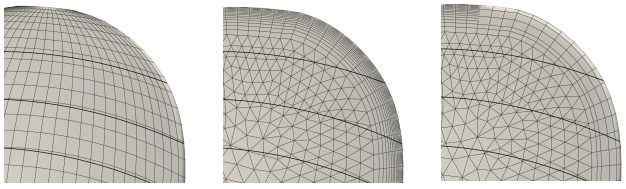

(a) Structured **(b) Unstructured** **(c) Coarsening**

Figure 2: E779A trailing edge coarsening

The geometry of the PPTC propeller is depicted in Figure 3 for a structured and an unstructured topology. The blade tip is trimmed at a relative radius $r/R = 0.9933$ for the structured grid and at a relative radius

of $r/R = 0.9910$ for the unstructured grid to allow better convergence for the nonlinear Kutta condition.

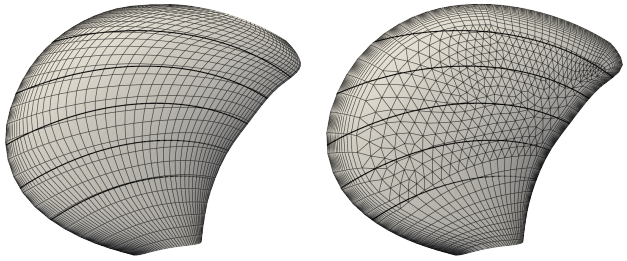

(a) Structured grid **(b) Unstructured grid**

Figure 3: PPTC Topologies

Similar to the E779A propeller, an optional coarsening of the unstructured grid is applied to study a possible improvement of the nonlinear Kutta condition. The sharp trailing edge bending of the PPTC propeller is currently challenging for the presented hyperbolic extrusion algorithm, as the grid lines in marching direction tend to intersect each other with increasing marching distance. This issue may be related to the fact that the algorithm employs constant explicit and implicit smoothing coefficients (Chan & Buning 1994).

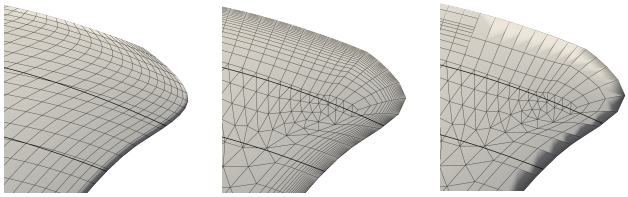

(a) Structured **(b) Unstructured** **(c) Coarsening**

Figure 4: PPTC trailing edge coarsening

The discretized hub surface with the hyperbolic grid and the advancing front grid is visualized in Figure 5, showing uniform panels especially around the blade-hub intersection.

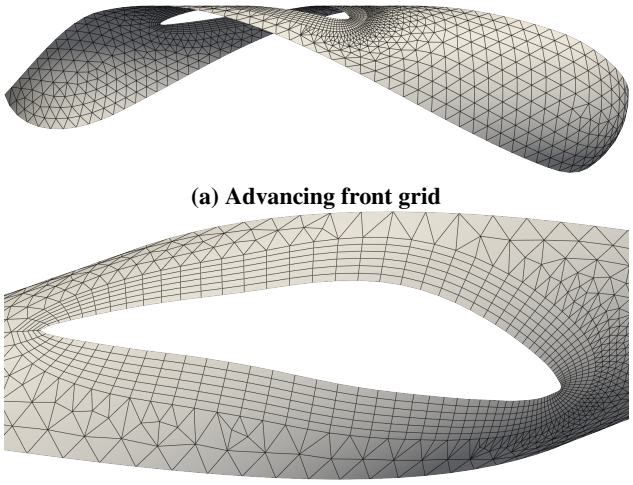

(a) Advancing front grid

(b) Hyperbolic grid

Figure 5: Hub surface discretization for the E779A propeller with periodic symmetry applied

4 RESULTS

In this section, the results of the gradient study and the open water performance prediction for the *Potsdam Propeller Test Case* (PPTC) and the *INSEAN Propeller E779A* are presented.

4.1 Surface Gradient Study

In the following, the different presented gradient polynomial ansatz functions and weighting functions for the surface gradient are explored for the PPTC propeller. To discuss the performance of the numerical solution the relative error between the analytical and numerical solution of the surface gradient is investigated by applying the test function

$$f(\boldsymbol{x}) = x^2 + y^2 + z^2 \quad \text{with}\, \boldsymbol{x} = (x, y, z)^T \ , \tag{1}$$

$$\boldsymbol{\nabla} f = (2x,\ 2y,\ 2z)^T \ . \tag{2}$$

The test function $f(\boldsymbol{x})$ and its gradient $\boldsymbol{\nabla} f$ are evaluated at each panel center to compare the different grids. The analytical gradients of the test function are calculated at the panel center and projected onto the panel surface to compare them with the numerical surface gradient reconstruction. Figure 6 shows the limited set of panels around the leading edge to evaluate the relative error since their influence is the largest for the structured grid (highly skewed panels of the structured grid towards the tip of the blade).

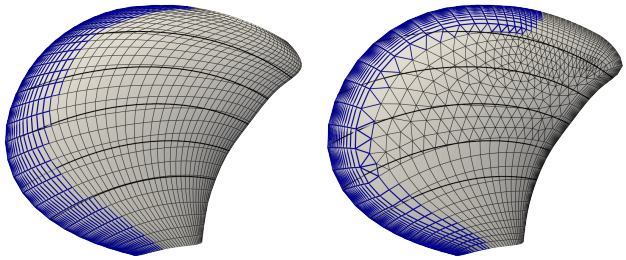

(a) Structured **(b) Unstructured**

Figure 6: Influence of the hub on streamlines

A statistical evaluation of the relative error using histograms is made for the normalized panel count for two intervals. The first interval for the small error ranges from $0\,\%$ to $5\,\%$. The second interval for the large error ranges from $5\,\%$ to $50\,\%$. Figure 7 shows the relative error of the surface gradient for four structured grids with increasing refinement level and the unstructured grid. The number of panels with larger error decays faster for the unstructured grid.

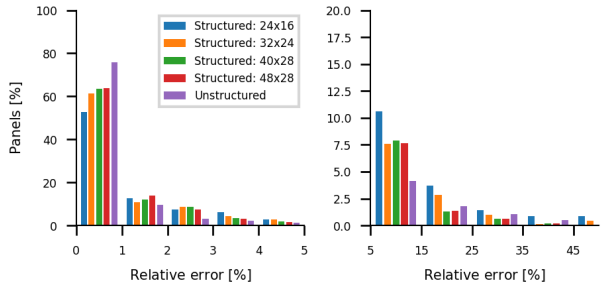

Figure 7: Comparison of structured and unstructured grid

About 80 % of the panels in the unstructured grid have a relative error below 1 %, while only 70 % of the structured grid fall within the same interval. Figure 8 shows the influence of the polynomial ansatz functions. The quadratic and biquadratic ansatz perform better than the others, but a considerable portion of the unstructured panels for the linear and bilinear case have large errors above 5 %.

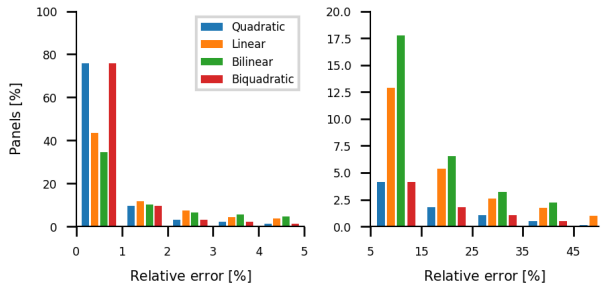

Figure 8: Gradient method influence on unstructured grid

Figure 9 shows the relative error of the quadratic ansatz polynomial function with varied weighting functions. Here, only the direct panel neighbors across the panel edges are considered. As the histogram shows, the influence of the weighting method is negligible.

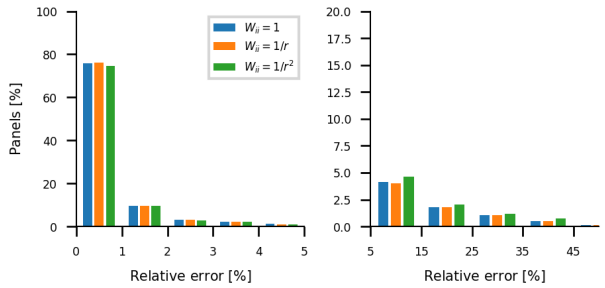

Figure 9: Gradient weight influence on unstructured grid

Finally, the gradient methods and weights are analyzed by including the neighboring panels at the panel corners. Figure 10 and 11 show the results, respectively. According to the presented results, it can be concluded, that the biquadratic method provides more accurate results than the quadratic ansatz if corner neighbors are included. Nevertheless, the number of panels within the smallest interval (0 % to 1 %) are reduced (around 70%) compared to the case in Figure 10 when no panel corner neighbors are included (around 80%).

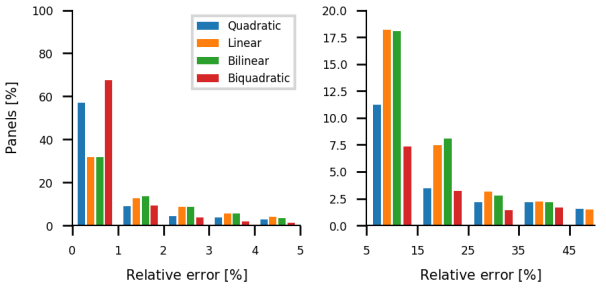

Figure 10: Corner neighbour influence on gradient methods

A similar trend is observed for the distance weighting functions in Figure 11. The inverse distance weighting significantly reduces the relative error with respect to unity weighting. The overall panel count with low relative error is smaller in the range up to 1 %, that is, between 55 % and 65 % of the panels, than for the case in Figure 9, where corner neighbors are not included ($\approx$ 75 % of the panels for all weights).

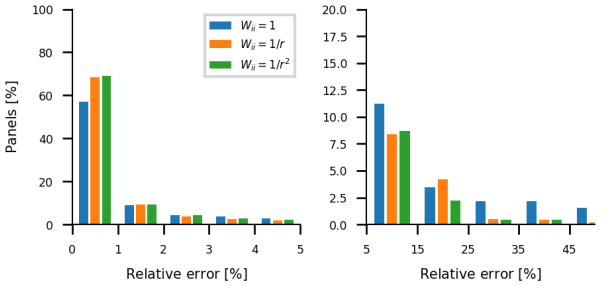

Figure 11: Corner neighbor influence on gradient weights

Summarized, the quadratic and biquadratic method provide higher accuracy than the linear and bilinear ansatz. In the case that the neighbors at the panel corners are included, a biquadratic approach with inverse distance weighting is recommended despite of the computational effort.

4.2 Open Water Test Comparison

The open water test simulations are carried out with a steady state algorithm and periodic boundary condition for taking into account the interaction with the neighbor blades. Instead of inserting new wake panels at the trailing edge every iteration, the doublet strength on the wake panels is updated. The shape of the wake sheet is initialized as a helix and iteratively updated until convergence.

At the blade tip, stability issues can arise due to high induced velocities. The wake panel roll-up may cause that the wake panels at the tip intersect the blade body panels, resulting in a singularity by the evaluation of the induced velocity. To mitigate this issue, the blade is slightly trimmed at the tip. Furthermore, the discrete grid with constant doublet strength distribution results in a jump of doublet strength, especially along the trailing edge direction. This jump represents a line vortex with constant strength. At the blade tip, this may lead to a locally non-uniform varying induced velocity distribution. By introducing the desingularization radius r_δ, the evaluation of induced velocities for

points close to the vortex axis are computed by a Lamb-Oseen-like vortex instead of a potential vortex. Choosing a suitable desingularization radius can introduce high uncertainty, since large values damp the wake deformation and prevent correct wake alignment. Hence, difficulties arise when different desingularization radii must be chosen for a wide range of advance ratios and different geometries, especially in the field of propeller optimization.

4.2.1 INSEAN Propeller E779A

An exemplary converged solution of the simulation setup for the advance ratio of $J = 0.88$ for propeller with hub is shown in Figure 12. The trailing edge of the panel connected to the hub surface is excluded from the wake shedding panel list to ensure that no wake panels intersect the hub panels.

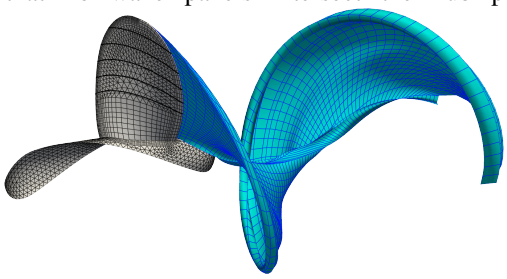

Figure 12: Converged open water result (E779A)

The open water diagram for a series of structured grids with three refinement levels is shown in Figure 13. The structured grid resolution is indicated by the number of panels in chordwise and spanwise direction, i.e. NC $\times$ NS. If the hub is included it is abbreviated with "w.Hub" else "w/o.Hub". The linear Kutta condition is abbreviated with "l.K" and the nonlinear Kutta condition with "n.l.K", respectively. The relative errors for the thrust coefficient and the torque coefficient with respect to the reference values at design point as discussed in Section 2 are also shown in the sub-figures below. The two coarser chord-wise and spanwise resolutions are studied with discretized hub and with nonlinear Kutta condition enabled. For the grid with the highest resolution also two evaluations (pastel colors) without hub and linear Kutta condition are carried out to study their effect on the solution. Regarding the coarser grid resolution, convergence can be observed with increasing chord resolution. Without applying the nonlinear Kutta condition, the error is slightly increased for k_T and k_Q except for small advance ratios. With the nonlinear Kutta condition applied, a considerable improvement of the relative error is visible. Yet, at low advance ratios, the trend of the torque is underpredicted independent of the applied grid.

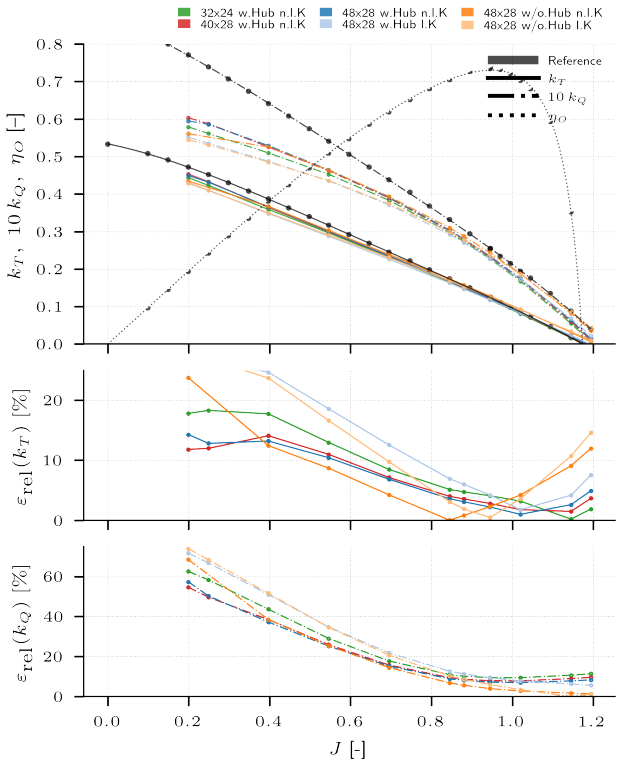

Figure 13: Open water diagram for E779A using structured grids of increased resolution with linear or nonlinear Kutta condition and with or without hub

In a next step, the structured grid with highest resolution is taken as a benchmark for the unstructured topology. The open water test is, again, evaluated for linear and nonlinear Kutta condition with and without hub and shown in Figure 14. The unstructured grid is abbreviated with "US.". Optional trailing edge coarsening is applied to investigate if homogeneous panel sizes with respect to the wake panel size can improve the convergence rate of the nonlinear Kutta condition. The unstructured grid with coarsening applied is indicated with "US.C". As expected, an improvement is visible when applying the nonlinear Kutta condition, but only with trailing edge coarsening. With nonlinear Kutta condition and hub included, the results show higher deviation from the experimental data than with linear Kutta condition. This may be related to the trailing edge located directly at the hub, at which wake panels are shed. This ensures a gap between hub surface and free shear sheet wake panels to suppress interaction between them. In contrast, without coarsening and nonlinear Kutta condition a clear deterioration even at high advance ratios is observed. With linear Kutta condition the results are considerably improved especially at low advance ratios. The error is still relatively large for the torque, but the difference between the predicted torque and the experimental data is reduced compared to the cases where the nonlinear Kutta condition is applied. In this case, the hub influence is negligible for the overall open water characteristics.

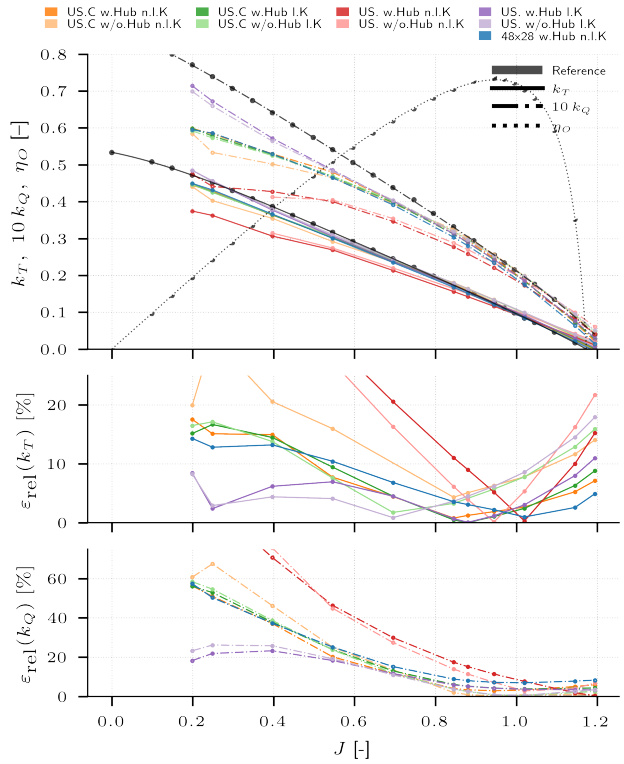

Figure 14: Open water diagram for E779A using unstructured grids with linear or nonlinear Kutta condition, with or without hub and with optional trailing edge coarsening

The influence of the hub on the streamlines, and hence on the Reynolds number Re and the prediction of viscous forces is shown in Figure 15. As can be seen the hub geometry ensures that the streamlines cannot circulate around the enclosing panels of the blade without hub.

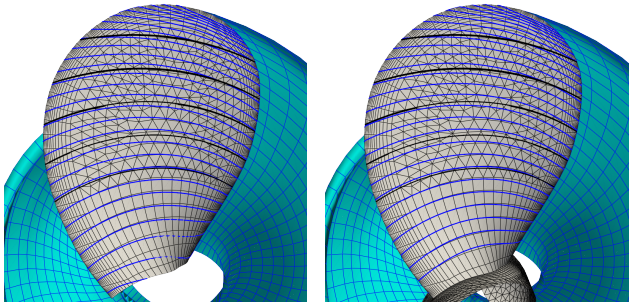

(a) Without hub **(a) With hub**

Figure 15: Influence of the hub on the streamlines

Finally, the pressure distribution is studied for representative sections. In Figure 16 the influence of the hub on the pressure distribution is shown for the structured grids. As stated before, the first trailing edge does not shed any wake panels. This is assumed to be the reason why the pressure distribution differs at the trailing edge ($c = 1.0$) considerably compared to the case without hub. For higher relative radii the difference between the pressure distributions becomes negligible.

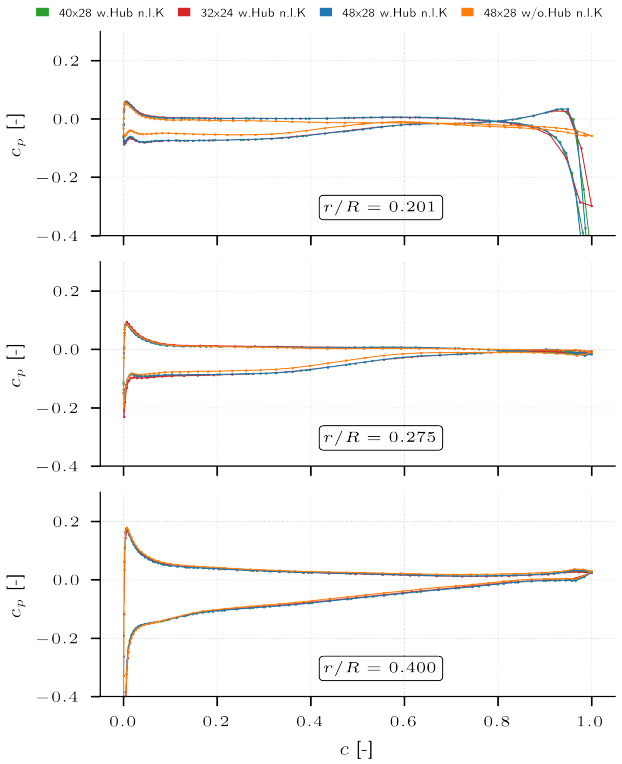

Figure 16: Hub influence on pressure distribution for the INSEAN E779A propeller at $J = 0.397$

Figure 17 shows the pressure distributions of the unstructured grid. Without hub the region around $c = 1.0$ show similar pressure levels independent of coarsening. Without coarsening a larger gradient in the pressure distribution in this region is seen. With the hub included, a large pressure drop at the trailing edge is present regardless of the Kutta condition employed. With increasing distance to the hub, the pressure distribution differences diminish except for the case with nonlinear Kutta condition, e.g. at $r/R = 0.3$. At larger relative radii, the unstructured grid shows fluctuations of the pressure distribution indicated by the pressure slice at $r/R = 0.7$ and 0.85. This effect does not occur for the structured grid; hence, it is assumed that the fluctuations are caused by the interpolation on the triangular topology. The deviation at the trailing edge for the grid without coarsening may be induced by the nonlinear Kutta condition due to the high aspect ratio of body panels compared with the wake panels. Therefore, coarsening the body panels at the trailing edge improves the convergence behavior. Applying the linear Kutta condition without coarsening leads to a reduction of the pressure difference between suction and pressure side, confined to a small chordwise region compared to the nonlinear Kutta condition without coarsening.

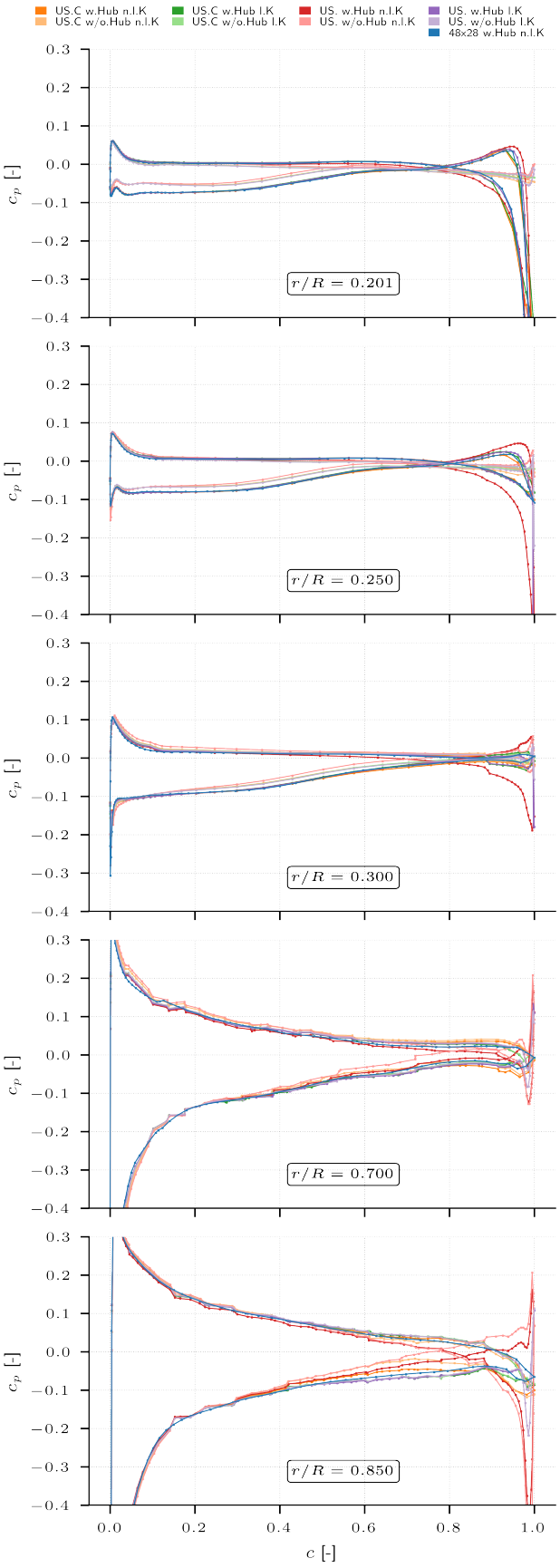

Figure 17: Unstructured grid influence on pressure distribution for the INSEAN E779A propeller at $J = 0.397$

4.2.2 Potsdam Propeller Test Case (PPTC)

For the evaluation of the applicability of the above mentioned approaches a second geometry, the PPTC propeller, is considered. An exemplary converged solution for the advance ratio of $J = 0.8$ for propeller with hub is shown in Figure 18. An influence of the hub on the wake panels can be seen, leading to a different wake alignment behavior.

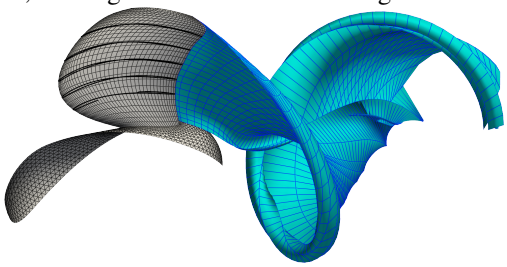

Figure 18: Converged open water result (PPTC)

Due to the relative higher skew in comparison to the E779A propeller the influence of the hub on the streamlines is more pronounced as shown in Figure 19.

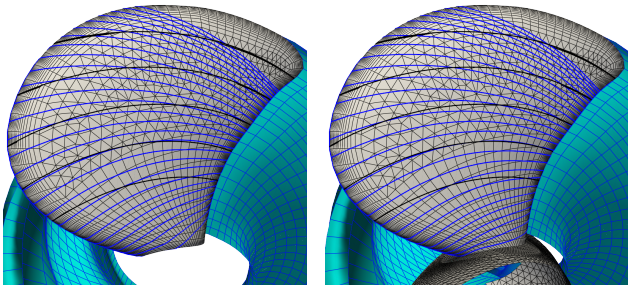

(a) Without hub **(a) With hub**

Figure 19: Influence of the hub on streamlines

The open water diagram is evaluated in a similar manner, for three structured grids as shown in Figure 20 and in comparison with the structured grid in Figure 21.

For the structured grids convergence improves with increasing the resolution. The span-wise refinement has a larger impact than the chord-wise resolution at small advance ratios. Without applying the nonlinear Kutta condition, the offset to the experimental results is considerably larger then with the nonlinear Kutta condition. Close to the design point, the open water characteristics are sufficiently predicted. Overprediction of the thrust takes place for large advance ratios, while small advance ratios are underpredicted. The propeller hub inclusion improves the results slightly but is small compared to the impact of nonlinear Kutta condition.

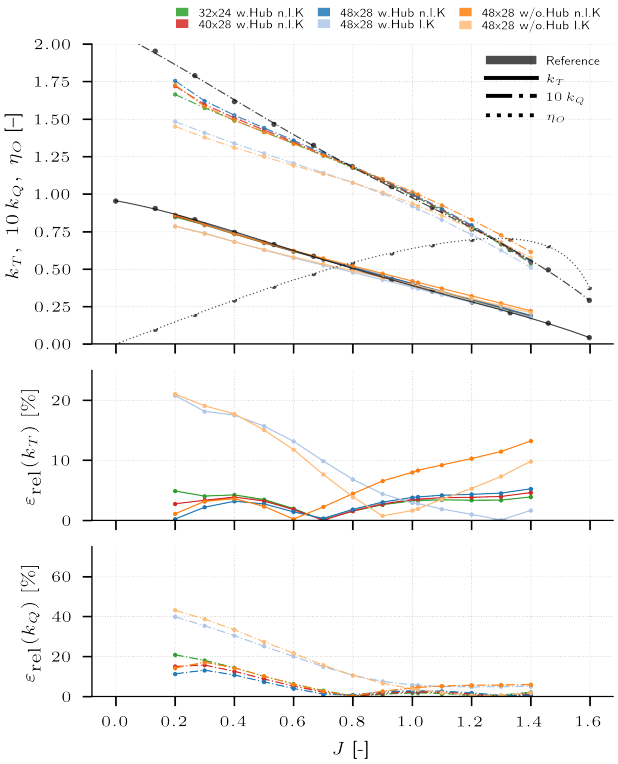

Figure 20: Open water diagram for PPTC using structured grids of increased resolution with linear or nonlinear Kutta condition and with or without hub

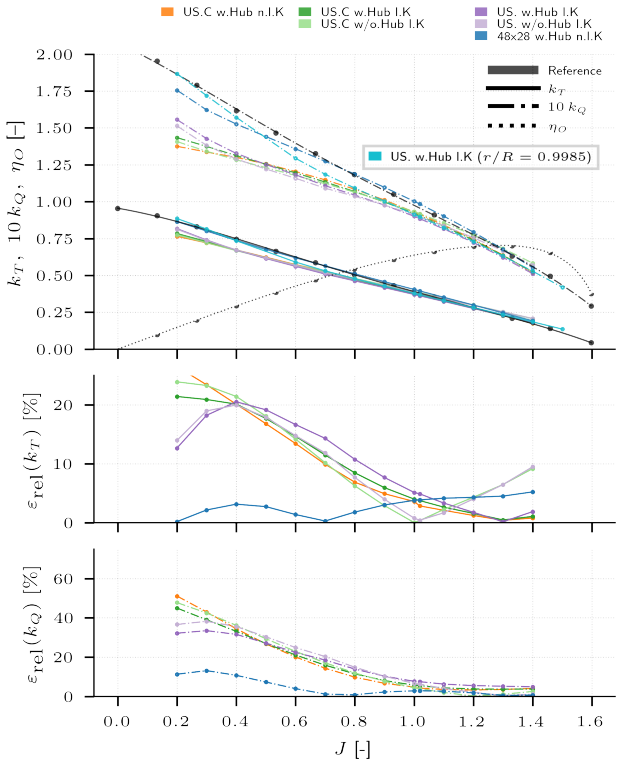

Figure 21: Open water diagram for PPTC using unstructured grids with linear or nonlinear Kutta condition, with or without hub and with optional trailing edge coarsening

The results of the unstructured grid in comparison to the reference case of the structured grid is shown in Figure 21. Compared to the E779A propeller not all computations for the PPTC are succeeded. Without grid coarsening the nonlinear Kutta condition could not be applied. Therefore these simulations are not included. The inclusion of the hub allows the computation of the flow using the unstructured grid with the nonlinear Kutta condition applied, hence, the hub improved the numerical stability of the simulation. With the linear Kutta condition and coarsening applied, a moderate improvement of predicting k_T and k_Q is achieved. The cases with linear Kutta condition performed considerably better than the cases with coarsening for small advance ratios. For larger advance ratios the prediction shows higher deviations.

As a large portion of the blade tip was trimmed to allow the nonlinear Kutta condition to converge, an additional evaluation with linear Kutta condition, hub included, and less blade tip trimming is provided at $r/R = 0.9985$. The torque coefficient is considerably improved just by less trimming the blade tip. At larger advance ratios, the structured grid shows a smaller deviation from the experimental data. At smaller advance ratios, the structured grid shows a higher deviation.

Thus, it can be stated that to improve the accuracy of the prediction at small advance ratios and to meet the slope of the torque coefficient curve, tip trimming should be kept as small as possible. However, less trimming causes stability issues when the nonlinear Kutta condition is applied.

Finally, the pressure distribution for the unstructured grids at the hub region is given in Figure 22. Likewise to the results obtained for the E779A propeller, the pressure at the trailing edge is influenced by the missing wake panel shedding. Nevertheless, at the leading edge a considerable influence is visible compared to the E779A propeller pressure distribution from Figure 16 which should not be influenced by the trailing edge wake panel issue. With increasing relative radii, the hub influence diminishes. Although it may only show moderate improvements in predicting thrust and torque coefficients, including the hub grid is important for a reliable prediction the onset of sheet cavitation close to the hub.

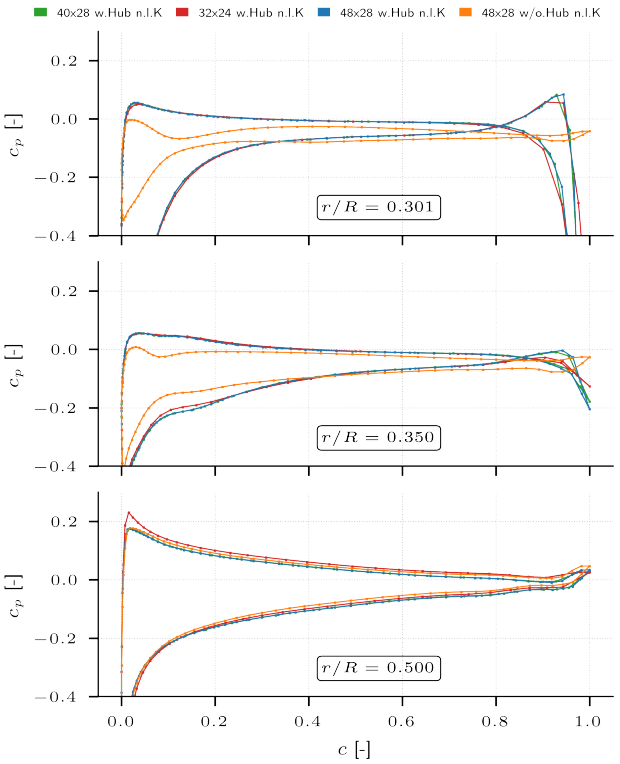

Figure 22: Hub influence on pressure distribution for the PPTC at $J = 0.4$

For the comparison of the pressure distribution between structured and unstructured grids Figure 23 is given. Coarsening at the trailing edge with using the linear Kutta condition introduces large pressure jumps at $c = 1$. The unstructured grid without hub achieves a pressure difference of almost zero, while with hub the pressure is, as described before, erroneous. The structured grid pressure distribution for suction and pressure side cross each other at the trailing edge region while without hub this is not the case, see Figure 22.

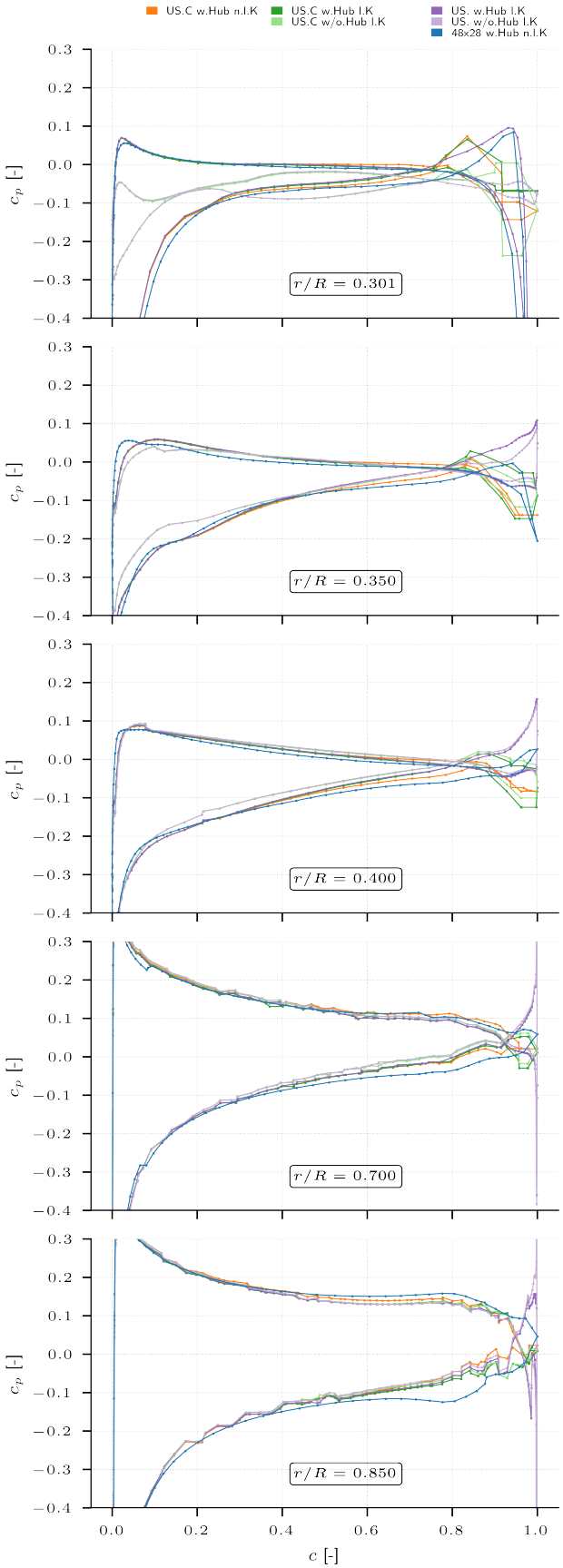

Figure 23: Unstructured grid influence on pressure distribution for the PPTC at $J = 0.4$

5 SUMMARY AND CONCLUSION

A boundary element code has been applied to calculate the open water characteristics of two representative propellers, the *INSEAN Propeller E779A* and the *Potsdam Propeller Test Case* (PPTC). The focus of this study was to investigate the influence of an unstructured grid topology, the hub and the nonlinear Kutta condition.

The chosen mesh topologies were described, followed by an assessment of different ansatz functions to calculate the surface gradients. Open water simulations for a set of structured and one unstructured grid were carried out. The resulting open water diagrams were compared with experimental data. The pressure coefficient across different radial cuts were compared for different setups to analyze the influence of grid topology, hub and Kutta condition. The uncertainty of picking a desingularization radius and its influence on wake alignment were discussed.

The stability of the nonlinear Kutta condition improved with the inclusion of the hub geometry as flow around the blade root is prevented. However, since not the entire trailing edge was shedding wake panels, flow from pressure to suction side resulted. The pressure coefficient slices along the chord have shown fluctuations when triangulated panels on the unstructured grid were evaluated. Since surface gradients are calculated with a quadratic polynomial ansatz without distance weighting, a possible improvement is given by considering panel corner neighbours and a biquadratic ansatz. The discretized propeller hub showed a significant influence on the pressure distribution. Thus, it is recommended to be included when the inception of sheet cavitation is of interest. For open water tests its influence is moderate. Care has to be taken at the trailing edge, i.e. suitable handling of wake panel shedding is necessary near the hub. It has been shown, that blade trimming must be reduced to a minimum to be able to predict the torque at low advance ratios accurately. Further improvements of the hyperbolic grid mesh generation are planned to increase the reliability of the meshing approach, especially for high skew propellers and zones with high curvature along the tip, e.g., by using locally varying smoothing coefficients.

Constant strength panel methods may be limited due to the artificial vortices induced by trailing wake panel edges in stream direction. Higher order panel methods can avoid this as continuous doublet distributions do not induce vortices originating from doublet strength jumps. The issue of the wake panel gap at the trailing edge could be avoided by using vortex particles instead of the panelised free shear sheet. Open water tests with this method were already studied by Wang & Abdel-Maksoud et al. (2017b) and showed promising results. Still, handling of the interaction with downstream or close-by bodies, e.g. the hub surface, need to be carefully considered in adequate boundary conditions.

6 ACKNOWLEDGEMENTS

The presented work was carried out as part of the German national research project *Red-Emi*, Reduction of hydroacoustic emissions from propulsion systems (“Reduktion der hydroakustischen Emission von Propulsionssystemen”). The project is funded by the German Ministry of Economic Affairs and Climate Action (BMWK) on the orders of the German Bundestag and PTJ as the conducting agency (FKZ 03SX560A).

REFERENCES

Chan, W. & P. Buning (1994). A hyperbolic surface grid generation scheme and its applications. In: *Fluid Dynamics Conference*. American Institute of Aeronautics and Astronautics.

Hundemer, J. (2013). Entwicklung eines Verfahrens zur Berechnung der instationären potenzialtheoretischen Propellerumströmung. de. PhD thesis.

Joseph Katz, A. P. (2010). Low-Speed Aerodynamics. Cambridge University Press. 630 pp.

Potsdam, S.-V. (2011). Potsdam Propeller Test Case (PPTC) - Open Water Tests with the Model Propeller VP1304. URL: https://www.sva-potsdam.de/wp-content/uploads/2016/04/SVA_report_3752.pdf (visited on 08/01/2023).

Rypl, D. & Z. Bittnar (1996). Direct triangulation of 3D surfaces using the advancing front technique. In: *Proceedings of the Second ECCOMAS Conference on Numerical Methods in Engineering*.

Salvatore, F. et al. (2006). Description of the INSEAN E779A Propeller Experimental Dataset. en.

Schlichting, H. (1979). Boundary-layer theory. New York: McGraw-Hill.

Wang, Y. et al. (2016). Prediction of tip vortex cavitation inception with low-order panel method. In: *Ocean Engineering* 125, pp. 124–133.

Wang & Abdel-Maksoud et al. (2017a). A fast method to realize the pressure Kutta condition in boundary element method for lifting bodies. In: *Ocean Engineering* 130, pp. 398–406.

– (2017b). Simulating marine propellers with vortex particle method. In: *Physics of Fluids* 29.1.